

Sequential multi-dimensional parameter inversion of induction logging data

Saputera, Durra H.; Jakobsen, Morten; van Dongen, K. W.A.; Jahani, Nazanin

DOI

[10.1111/1365-2478.70017](https://doi.org/10.1111/1365-2478.70017)

Publication date

2025

Document Version

Final published version

Published in

Geophysical Prospecting

Citation (APA)

Saputera, D. H., Jakobsen, M., van Dongen, K. W. A., & Jahani, N. (2025). Sequential multi-dimensional parameter inversion of induction logging data. *Geophysical Prospecting*, 73(4), 1315-1332.
<https://doi.org/10.1111/1365-2478.70017>

Important note

To cite this publication, please use the final published version (if applicable).
Please check the document version above.

Copyright

Other than for strictly personal use, it is not permitted to download, forward or distribute the text or part of it, without the consent of the author(s) and/or copyright holder(s), unless the work is under an open content license such as Creative Commons.

Takedown policy

Please contact us and provide details if you believe this document breaches copyrights.
We will remove access to the work immediately and investigate your claim.

Green Open Access added to TU Delft Institutional Repository

'You share, we take care!' - Taverne project

<https://www.openaccess.nl/en/you-share-we-take-care>

Otherwise as indicated in the copyright section: the publisher is the copyright holder of this work and the author uses the Dutch legislation to make this work public.

Sequential multi-dimensional parameter inversion of induction logging data

Durra H. Saputera¹  | Morten Jakobsen¹  | K. W. A. van Dongen² | Nazanin Jahani³

¹Department of Earth Science, University of Bergen, Bergen, Norway

²Department of Imaging Physics, Delft University of Technology, Delft, The Netherlands

³Energy Department, NORCE Norwegian Research Centre, Bergen, Norway

Correspondence

Durra H. Saputera, Department of Earth Science, University of Bergen, Bergen, 5020, Norway.

Email: durra.saputera@uib.no

Funding information

Norges Forskningsråd (The Research Council of Norway); Center for Research-Based Innovation DigiWells: DigitalWell Center for Value Creation Competitiveness and Minimum Environmental Footprint, Grant/Award Number: NFR SFI project no. 309589

Abstract

Structural information about the subsurface near the borehole can be obtained from reconstructed conductivity distributions. These distributions may be reconstructed via the inversion of deep-sensing electromagnetic induction log data. Unfortunately, these complex media often display anisotropy and structural variations in both horizontal and vertical directions, making the three-dimensional inversion computationally demanding and ill-posed. To address these challenges, we introduce a sequential inversion strategy of deep-sensing electromagnetic induction logging data that is measured while drilling. For the inversion at each logging position, we employ a matrix-free implementation of the adjoint integral equation method and a quasi-Newton algorithm. To tackle the ill-posed nature of the problem, we regularize the inverse problem by employing a multi-dimensional inversion parameter technique that shifts from zero- to three-dimensional parameterization. The model derived from the inversion of the data at multiple positions is incrementally integrated by utilizing the sensitivity data at each logging position. To validate our approach, we tested our method on simulated data using an anisotropic model. These experiments show that this approach produces a good reconstruction of the true conductivity for the whole track while only doing the inversion at a single position at a time.

KEY WORDS

anisotropy, electromagnetics, inversion, integral equation method, mathematical formulation, numerical study

INTRODUCTION

The tri-axial deep-sensing electromagnetic (EM) induction tool is frequently deployed by the industry for characterizing the subsurface around the borehole to achieve an optimal well-placement (Antonsen et al., 2022; Omar et al., 2024; Sviridov et al., 2023). Throughout the time, the inversion EM induction tool has advanced from one-dimensional (1D) into three-dimensional (3D) inversion (Clegg et al., 2021). With the advancement of EM induction log 3D inversion, electrical conductivity variations in the azimuthal and vertical directions can be obtained through the inversion to derive the geological information about the subsurface around the

borehole. Additionally, all nine components acquired by the tool can be utilized in the 3D inversion for improved lithology differentiation and fluid boundaries detection (Alkhars et al., 2022; Clegg et al., 2021). With an optimized inversion algorithm, it is possible to get inversion results within a few minutes, enabling real-time monitoring for geosteering application (Elkhamry et al., 2023; Wilson et al., 2019). Although this is the case, the 3D inversion is still computationally challenging and the 1D inversion is still widely applied for real-time applications due to the lower computational cost needed for the 1D inversion compared to the 3D inversion (Sviridov et al., 2023; Wu et al., 2024). The limitation is that 1D inversions may fail to converge below a specified data

misfit goal in the presence of lateral heterogeneities (Omar et al., 2024; Saputra et al., 2024). This motivates the development of an efficient inversion workflow for EM induction log inversion while drilling using 3D forward modelling.

Forward modelling of 3D EM fields is the most intensive part of the inversion process (Yang, 2023) and one of the main challenges for 3D inversion. For deterministic inversion, forward modelling is not only needed for calculating the EM fields measured at the receiver positions but also to calculate the gradient of the objective function. Although there are different methods for numerical simulation of 3D EM data, they all obtain the EM fields by solving a linear system of equations after discretization of the surrounding subsurface (Newman & Alumbaugh, 2002; Wang et al., 2021). Iterative methods are the way to go for solving a linear system of equations with a large number of grid points using a limited amount of computational resources. These methods in combination with the adjoint method allow for matrix-free implementation of the inversion algorithm (Jakobsen et al., 2023; Yang, 2023). Following this approach, it becomes feasible to do a 3D inversion on a desktop computer.

Another main challenge is the ill-posed nature of the 3D inversion problems. Typically, the induction tool data may not uniquely determine the subsurface structure due to the limited sensitivity and resolution of the tool at each logging position. This is especially the case when anisotropy needs to be taken into account as this would mean that even more unknowns need to be taken into account (Elkhamry et al., 2022). To overcome the aforementioned challenges, regularization becomes an important part of the inversion process. Regularization is typically done by introducing penalty terms into the objective function to stabilize the inversion process. These extra terms may be included either additively or multiplicatively (Jakobsen & Tveit, 2018; Van den Berg & Abubakar, 2001; Yang, 2023). The complexity of regularization increases when dealing with multi-parameter inversion, where multiple regularization parameters are required to obtain a more favourable result. To mitigate this problem, some studies approach the problem by starting the inversion from a homogeneous or 1D conductivity inverse and use the obtained results as an initial model for the two-dimensional (2D) or 3D inverse problem, progressively (Omar et al., 2024; Saputra et al., 2024).

In this work, we adapt the anisotropic inversion with multi-dimensional parameters within the 3D inversion framework for a logging-while-drilling scenario where the data are inverted sequentially along the well trajectory. To generate a consistent description of the inverted model, we introduce the separation between the forward modelling window and the inversion grid. The forward modelling window is only defined within the sensitivity range of the induction tool at each logging position. The inversion grid is defined globally over the entire spatial domain that covers the local forward modelling windows. The conductivity values inside these windows are

connected through a mapping operation from the inversion grid, which we recast as the summation of basis functions with different magnitudes. The conductivity profile defined in the inversion grid is used as the initial model of the inversion process at each logging position, and it is continuously updated as the data from a new logging point is introduced.

In each inversion process, we use the limited-memory Broyden–Fletcher–Goldfarb–Shanno (L-BFGS) algorithm (Liu & Nocedal, 1989) to minimize the defined objective function. Our formulation is based on the integral equation method, which is implemented in a matrix-free manner to efficiently compute the forward modelling and gradient of the objective function (Jakobsen et al., 2023). We parameterize the anisotropic conductivity as a combination of anisotropic parameters to couple the update of different conductivity components in the inversion process. Additionally, we combine it with the usage of trigonometric functions (Abubakar et al., 2006) to limit the search space of the conductivity values and therefore stabilize the inversion process. To help mitigate the ill-posed problem in the inverse process, we employ a multi-dimensional inversion workflow where we start inverting for homogeneous anisotropic values (0D) and only start to introduce higher dimensionality (1D, 2D, then 3D) conductivity profiles when the data misfit goal is not reached.

In the deterministic inversion framework, the initial conductivity model for the inversion of a new data point is updated directly using the prior inversion results. As inverted model parameters from different data points can have different dimensionalities in our proposed inversion workflow, this approach will result in the loss of information about the dimensionality of the inverted parameters from the past data points in the sequential process. Therefore, we assimilate the inversion results from multiple logging positions into a single conductivity model through weighted averaging based on the sensitivity of the tool at each position. Afterwards, this assimilated conductivity is used to determine the initial model of the inversion at the new data point.

The structure of this paper is as follows. We begin with a detailed discussion of the theoretical framework of our inversion method in the second section. This is followed by two numerical experiments in the third section that demonstrate the performance of our inversion approach. In the first example, we consider a simple horizontally layered model with vertical transverse isotropy (VTI) where the data are generated from a semi-analytical 1D code (Shahriari et al., 2018) to test the robustness of our approach in the presence of a numerical model error. Additionally, we use this model to investigate the effect of using different anisotropy types in the inversion parameters. In the second example, we show an inversion case across a VTI formation with lateral heterogeneities due to the presence of faults. We show that our inversion scheme is able to adapt to 2D parameterization. Lastly, we present a

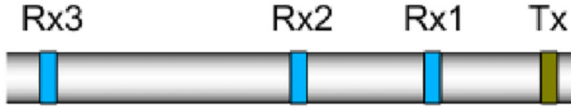


FIGURE 1 Sketch of electromagnetic induction tools with Tx and Rx indicate the transmitter and receiver positions.

discussion of the implications of our findings and conclude with a summary of our contributions and potential avenues for future research in the last section.

THEORY

For the application of our work, we consider a triaxial induction logging tool as illustrated in Figure 1. The tool consists of transmitters and receivers orientated in three orthogonal directions, with the z-component coils pointing in the drilling direction. The transmitters emit the magnetic field of certain frequencies from a single location, which is captured by the receivers located behind the transmitters in the drilling direction (Antonsen et al., 2022).

Forward model

In the theory for modelling, the induction tools' response is governed by the Maxwell's equations for heterogeneous media (Zhdanov, 2009) within the frequency domain:

$$\nabla \times \mathbf{e}(\mathbf{x}, \omega) = i\omega\mu_0 \mathbf{h}(\mathbf{x}, \omega) + \mathbf{j}^H(\mathbf{x}, \omega), \quad (1)$$

$$\nabla \times \mathbf{h}(\mathbf{x}, \omega) = \hat{\sigma}(\mathbf{x}, \omega) \mathbf{e}(\mathbf{x}, \omega), \quad (2)$$

where $\mathbf{e}(\mathbf{x}, \omega)$ and $\mathbf{h}(\mathbf{x}, \omega)$ denote the electric and magnetic fields, respectively. $\mathbf{j}^H(\mathbf{x}, \omega)$ denotes the term of the magnetic source, ω is the angular frequency and \mathbf{x} is the position vector in the three-dimensional (3D) space \mathbb{R}^3 . $\hat{\sigma}(\mathbf{x}, \omega) = \sigma(\mathbf{x}) - i\omega\epsilon(\mathbf{x})$ is the complex electric conductivity, $\epsilon(\mathbf{x})$ is the dielectric permittivity and $i = \sqrt{-1}$ is the imaginary unit. We assume a constant magnetic permeability equal to the magnetic permeability of the vacuum μ_0 . Additionally, we consider that the tool works in the diffusion regime where the contribution of the dielectric permittivity in the imaginary part of the complex conductivity is ignored, and $\hat{\sigma}(\mathbf{x}, \omega) = \sigma(\mathbf{x})$ for all the tool operating frequencies.

We use an integral equation (IE) method to compute the electric and magnetic fields. These fields can be expressed as the sum of a background and a scattered field, hence

(Zhdanov, 2009)

$$\mathbf{e}(\mathbf{x}, \omega) = \mathbf{e}^{(0)}(\mathbf{x}, \omega) + \int_{\Omega} \mathbf{G}^{(0,E)}(\mathbf{x}, \mathbf{x}', \omega) \Delta\sigma(\mathbf{x}') \mathbf{e}(\mathbf{x}', \omega) dV(\mathbf{x}'), \quad (3)$$

$$\mathbf{h}(\mathbf{x}, \omega) = \mathbf{h}^{(0)}(\mathbf{x}, \omega) + \int_{\Omega} \mathbf{G}^{(0,H)}(\mathbf{x}, \mathbf{x}', \omega) \Delta\sigma(\mathbf{x}') \mathbf{e}(\mathbf{x}', \omega) dV(\mathbf{x}'), \quad (4)$$

where $\mathbf{G}^{(0,E/H)}$ indicates the dyadic Green's function for the electric and magnetic field due to an electric source, respectively. The upper scripts (0) refer to the fields and Green's functions defined for the homogeneous isotropic background medium. Ω is the spatial domain with non-zero conductivity contrast $\Delta\sigma(\mathbf{x}) = \sigma(\mathbf{x}) - \sigma_0 \mathbf{I}$ with $\sigma(\mathbf{x})$ the conductivity tensor of the actual anisotropic medium, σ_0 is the homogeneous isotropic conductivity for the background medium and \mathbf{I} is the identity matrix. The dyadic Green's functions are defined as (Fang et al., 2006)

$$\mathbf{G}^{(0,E)}(\mathbf{x}, \mathbf{x}', \omega) = \left(i\omega\mu_0 \mathbf{I} + \frac{1}{\sigma_0} \nabla \nabla \right) g(\mathbf{x}, \mathbf{x}', \omega), \quad (5)$$

$$\mathbf{G}^{(0,H)}(\mathbf{x}, \mathbf{x}', \omega) = (i\omega\mu_0)^{-1} \nabla \times \mathbf{G}^{(0,E)}, \quad (6)$$

$$g(\mathbf{x}, \mathbf{x}', \omega) = \frac{e^{ik_0|\mathbf{x}-\mathbf{x}'|}}{4\pi|\mathbf{x}-\mathbf{x}'|}, \quad (7)$$

where $g(\mathbf{x}, \mathbf{x}', \omega)$ is the scalar Green's function with complex wavenumber $k_0 = \sqrt{i\omega\mu_0\sigma_0}$.

The electric field for the heterogeneous medium in Equation (3) is the solution of the following linear system of equations:

$$\left[\mathbf{I} - \mathcal{G}^{(0,E)} \Delta\sigma \right] \mathbf{e} = \mathbf{e}^{(0)}, \quad (8)$$

and

$$\mathbf{e}^{(0)} = \mathcal{G}^{(0,E)} \mathbf{j}, \quad (9)$$

where $\mathbf{j} = \nabla \times \mathbf{j}^H$ is the electric source vector and $\mathcal{G}^{(0,E)}$ is the operator that represents the convolution integral of the dyadic Green's function $\mathbf{G}^{(0,E)}(\mathbf{x}, \mathbf{x}', \omega)$. In this notation, we drop the dependency on variables for simplicity. Note that, to differentiate the convolution integral operations from the ordinary matrix-vector or vector-vector multiplication, we use a calligraphic font to denote the integral operators in the remainder of this work. Next, the calculation of the total

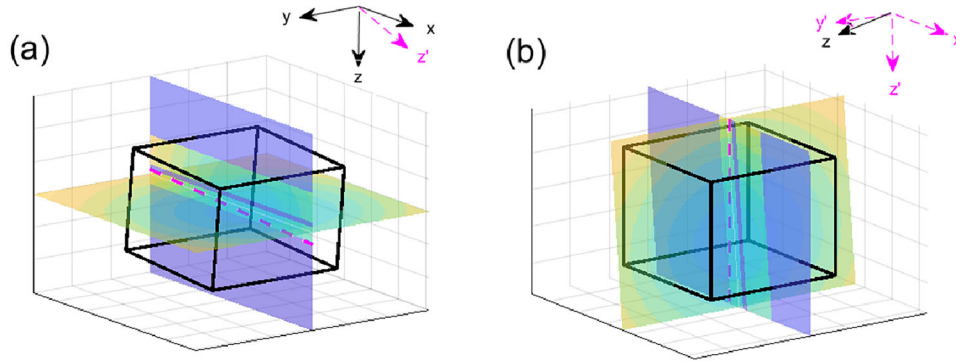


FIGURE 2 Sketch of forward modelling window in (a) the global Cartesian frame and (b) the rotated frame. The black and magenta arrows indicate the principal axes' direction. In both figures, the direction of z and z' are drawn to indicate the relative angle between the frames.

magnetic field is a straightforward summation of the background magnetic field and the scattered field as shown in Equation (4), written in the operator form as

$$\mathbf{h} = \mathbf{h}^{(0)} + \mathcal{G}^{(0,H)} \Delta \sigma \mathbf{e}, \quad (10)$$

where $\mathcal{G}^{(0,H)}$ is the convolution integral operator of the dyadic Green's function $\mathbf{G}^{(0,H)}(\mathbf{x}_r, \mathbf{x}', \omega)$. Here, the operator only computes the magnetic fields at the receiver positions \mathbf{x}_r , as the magnetic fields are only observed at these positions.

A numerical solution of Equations (8) and (10) can be obtained using the method of moments and discretizing the subsurface model around the induction tool into a set of cubic grid blocks (Gibson, 2021). To overcome problems with the singularity of the Green's function, we use its weak form for discretization with cubic grid blocks and calculate its singularity part by integrating the Green's function of a grid block over a spherical domain with equivalent volume (Jakobsen & Tveit, 2018; Zwamborn & Van Den Berg, 1992). The linear system in Equation (8) can be efficiently solved using a Krylov-subspace-based solver (Barrett et al., 1994; Saad, 2003). In this way, the discretized linear system can be formulated as operators, and there is no need to store it explicitly as a matrix. Furthermore, the usage of Fast Fourier Transform (FFT) to compute the convolution integral operator and preconditioners can be implemented to reduce the computation time (Fang et al., 2006).

For simulating logging while drilling scenario, we assume a moving 3D forward modelling window as illustrated in Figure 2. When performing the numerical calculation of the fields, we set a constant background conductivity for all windows and ignore the scattering fields far away from the tool position by setting zero conductivity contrast outside the window. Additionally, each forward modelling window is rotated such that the window's z -axis is in the drilling direction, which is also in the orientation of the z -component of the transmitter and coils. Due to this rotation, the conductivity tensor also needs to be rotated (Gao, 2006; Pardo & Torres-Verdín, 2015).

The conductivity of a general anisotropic medium can be written as a 3×3 symmetric tensor (Greenhalgh et al., 2009; Zhdanov, 2009). Due to its symmetry, it can be diagonalized and expressed via three principal values and a rotation matrix (Moran & Gianzero, 1979; Pek & Santos, 2002), consequently

$$\sigma(\mathbf{x}) = \mathbf{R}^T \begin{bmatrix} \sigma_1(\mathbf{x}) & 0 & 0 \\ 0 & \sigma_2(\mathbf{x}) & 0 \\ 0 & 0 & \sigma_3(\mathbf{x}) \end{bmatrix} \mathbf{R}, \quad (11)$$

where $\sigma_1(\mathbf{x})$, $\sigma_2(\mathbf{x})$ and $\sigma_3(\mathbf{x})$ are the principal conductivity values in the x , y and z directions, respectively, within the geological frame. The matrix \mathbf{R} denotes the rotation matrix, and T indicates the matrix transpose operation. The matrix \mathbf{R} transforms the coordinate system from the geological frame to the local frame with the axes in the direction of the tool coil orientation. It can be expressed as three elementary Euler's rotations with two rotation axes (Kong et al., 2021; Pek & Santos, 2002) or as three rotation axes (Rong et al., 2022; Yin, 2000). In this study, we follow the definition of the rotation matrix with two rotation axes (Pek & Santos, 2002), hence

$$\mathbf{R} = \mathbf{R}_z(\alpha_L(\mathbf{x})) \mathbf{R}_y(\alpha_D(\mathbf{x})) \mathbf{R}_z(\alpha_S(\mathbf{x})), \quad (12)$$

where the $\alpha_S(\mathbf{x})$, $\alpha_D(\mathbf{x})$ and $\alpha_L(\mathbf{x})$ are the rotation angles. $\mathbf{R}_y(\alpha)$ and $\mathbf{R}_z(\alpha)$ are the spatial dependent rotation matrices around the y - and z -axis, respectively, given by

$$\mathbf{R}_y(\alpha) = \begin{bmatrix} \cos(\alpha) & 0 & -\sin(\alpha) \\ 0 & 1 & 0 \\ \sin(\alpha) & 0 & \cos(\alpha) \end{bmatrix}, \quad (13)$$

$$\mathbf{R}_z(\alpha) = \begin{bmatrix} \cos(\alpha) & -\sin(\alpha) & 0 \\ \sin(\alpha) & \cos(\alpha) & 0 \\ 0 & 0 & 1 \end{bmatrix}. \quad (14)$$

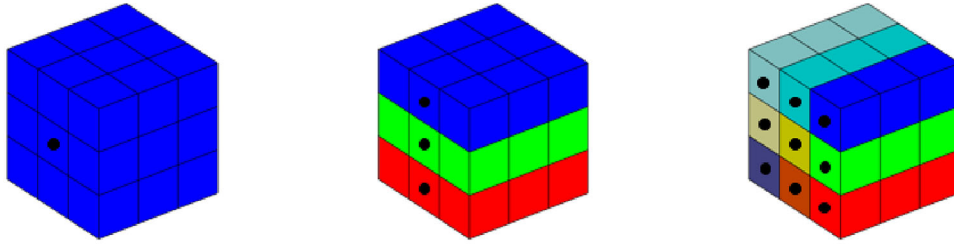


FIGURE 3 Sketch of conductivity mapping from inversion grid points into the 3D grid space. The dots represent inversion grid points of the 0D, 1D and 2D parameters from left to right.

The rotation angles $\alpha_S(\mathbf{x})$, $\alpha_D(\mathbf{x})$, and $\alpha_L(\mathbf{x})$ are related to the strike, dip and slant angles of the anisotropy, respectively (Pek & Santos, 2002). In this study, we assume that these angles are set to the drilling trajectory angles across the entire spatial domain.

Inverse problem

Model parameterization

For mapping the conductivity distribution in the spatial domain, the conductivity tensor is expressed as a sum of scaled basis functions

$$\sigma(\mathbf{x}) = \sum_{n=1}^N K^{(n)}(\mathbf{x}) \mathbf{C}^{(n)}, \quad (15)$$

where $K^{(n)}(\mathbf{x})$ indicates the basis function with spatial dependence, $\mathbf{C}^{(n)}$ is the conductivity tensor for the n th basis function and N is the total number of basis functions.

Using the definition with the basis functions, we control the dimensionality of the model parameters by defining the inversion grid points according to the desired dimension of the parameters. In this study, we use the block indicator function as the basis function

$$K^{(n)}(\mathbf{x}) = \begin{cases} 1 & \text{if } \mathbf{x} \in \Omega^{(n)}(\mathbf{x}) \\ 0 & \text{if } \mathbf{x} \notin \Omega^{(n)}(\mathbf{x}) \end{cases}, \quad (16)$$

where $\Omega^{(n)}(\mathbf{x})$ corresponds to a volume enclosed by the n th inversion grid block. The domain $\Omega^{(n)}$ is then determined from these grid points using the nearest neighbour algorithm, as illustrated in Figure 3. For homogeneous anisotropic parameter inversion (0D), a single centroid defined anywhere in the spatial domain is sufficient as the parameters are spatially invariant. Assuming a horizontally layered earth, one-dimensional (1D) parameter inversion grid points are defined along the z -axis with uniform spacing. The two-dimensional (2D) parameter inversion grid is subsequently

done by introducing more points along the x -axis of the 1D parameter inversion grid.

The forward modelling window is discretized into a set of uniform grid blocks in the 3D spatial domain for the numerical calculation of the electric and magnetic fields. As the logging position may not be spaced regularly, the grid points defined in different forward modelling windows may not coincide with each other. Therefore, we propose to define the inverted conductivity parameters on the global grid to create a consistent description of the conductivity distribution from multiple forward modelling windows. Figure 4 illustrates the mapping of the conductivity distribution from the global inversion grid to a local forward modelling window using the nearest neighbour interpolation algorithm.

Assuming that the angles of the rotation matrices in Equation (11) are known, the inversion task is to find the principal conductivity values. Instead of inverting for these quantities directly, we propose to define the principal conductivities as follows:

$$\begin{aligned} c_1^{(n)} &= \bar{\sigma} + \delta\sigma \sin \left[m_1^{(n)} \right], \\ c_2^{(n)} &= \bar{\sigma} + \delta\sigma \sin \left[m_1^{(n)} + m_2^{(n)} \right], \\ c_3^{(n)} &= \bar{\sigma} + \delta\sigma \sin \left[m_1^{(n)} + m_2^{(n)} + m_3^{(n)} \right], \end{aligned} \quad (17)$$

with the conductivity mid-point $\bar{\sigma}$ and half-range $\delta\sigma$ constant defined as

$$\bar{\sigma} = \frac{1}{2}(\sigma_{\max} + \sigma_{\min}), \quad (18)$$

$$\delta\sigma = \frac{1}{2}(\sigma_{\max} - \sigma_{\min}), \quad (19)$$

where σ_{\min} and σ_{\max} are the expected minimum and maximum values for the conductivity, respectively. $m_1^{(n)}$ is an isotropic angle with $m_2^{(n)}$ and $m_3^{(n)}$ the anisotropic perturbations in the other conductivity components. In this way, the

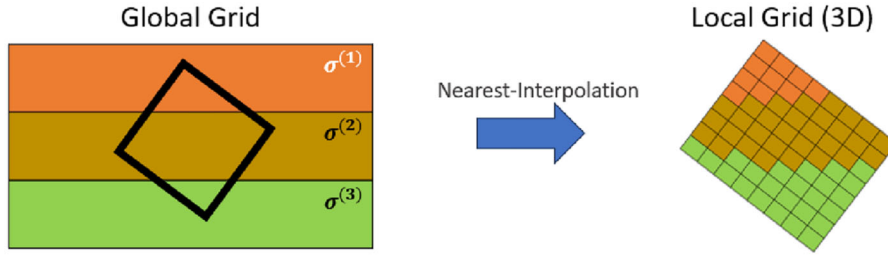


FIGURE 4 Example of mapping from global inversion grid to the forward modelling window in 2D-plane view. The black rectangle indicates the boundaries of the forward modelling window in the global grid.

updates of the principal conductivity values in the inversion are now coupled. When the measurement configuration is not sensitive to one of the principal values, its structural pattern will follow the isotropic perturbation. Additionally, the use of the sine function allows us to constrain the conductivity values within the range of σ_{\min} and σ_{\max} (Abubakar et al., 2008). These bounds can be determined using a priori knowledge and help to stabilize the inversion in a more physically sensible manner (Yang, 2023).

Combining the model parameter description in this section and including the tensor rotation in Equation (11), the conductivity tensor can be expressed using the model parameters in the following:

$$\sigma(\mathbf{x}) = \bar{\sigma}\mathbf{I} + \delta\sigma \sum_{n=1}^N K^{(n)}(\mathbf{x})\mathbf{R}^T \sin[\mathbf{M}^{(n)}]\mathbf{R}, \quad (20)$$

where $\mathbf{M}^{(n)}$ is the matrix containing the anisotropic model parameters to be inverted. For the derivation of the objective function gradient, it is convenient to write the matrix $\mathbf{M}^{(n)}$ in the form of (Jakobsen et al., 2023)

$$\mathbf{M}^{(n)} = \sum_{j=1}^3 \mathbf{P}^{(j)} m_j^{(n)}, \quad (21)$$

with matrices $\mathbf{P}^{(j)}$ given by

$$\mathbf{P}^{(1)} = \begin{bmatrix} 1 & 0 & 0 \\ 0 & 1 & 0 \\ 0 & 0 & 1 \end{bmatrix}, \mathbf{P}^{(2)} = \begin{bmatrix} 0 & 0 & 0 \\ 0 & 1 & 0 \\ 0 & 0 & 1 \end{bmatrix}, \text{ and } \mathbf{P}^{(3)} = \begin{bmatrix} 0 & 0 & 0 \\ 0 & 0 & 0 \\ 0 & 0 & 1 \end{bmatrix}. \quad (22)$$

With this formulation, we decompose the model parameters into their spatial-dependent part, tensorial part and scalar part. The gradient of the objective function is obtained by taking the derivative of the objective function with respect to the scalar part $m_j^{(n)}$. For the special case of vertical transverse isotropy (VTI) media where $\sigma_1 = \sigma_2$, we can simply set $m_2 = 0$. By additionally setting $m_3 = 0$, we get the special case of isotropic conductivity.

Objective function

A deterministic inversion algorithm tries to find the model parameters that minimize an objective function from given initial values. We define the objective function as the weighted sum of the squared magnitude of the data misfit for all receiver positions \mathbf{x}_r and all source configurations s (Van den Berg & Van der Horst, 1995), namely

$$\Phi_D = \frac{1}{2} \sum_s \sum_{\mathbf{x}_r} \left\| W(\mathbf{x}_r, s) \Delta \mathbf{h}(\mathbf{x}_r, s) \right\|_2^2, \quad (23)$$

with $\|\cdot\|_2$ the L2 norm and $\Delta \mathbf{h}$ the data misfit defined as

$$\Delta \mathbf{h}(\mathbf{x}_r, s) = \mathbf{h}^{(obs)}(\mathbf{x}_r, s) - \mathbf{h}(\mathbf{x}_r, s), \quad (24)$$

where $\mathbf{h}^{(obs)}(\mathbf{x}_r, s)$ and $\mathbf{h}(\mathbf{x}_r, s)$ are the observed and predicted model's calculated magnetic fields, respectively. The transmitter configuration s includes the transmitter position, orientation and frequency. The weight factor $W(\mathbf{x}_r, s)$ is used to normalize the data misfit with different configurations. In this study, we define the weights as the inverse of the magnetic field's magnitude of multiple orientations and frequencies at the receiver position:

$$W(\mathbf{x}_r) = \frac{1}{\sum_s \left\| \mathbf{h}^{(obs)}(\mathbf{x}_r, s) \right\|_2}. \quad (25)$$

We chose this specific weighting to equalize the magnitude of the data vector as the magnetic field is decaying away from the transmitter position. This weighting matrix may be adjusted accordingly based on tool configuration and to incorporate measurement uncertainty (Jahani et al., 2023).

In this study, we used the limited-memory Broyden–Fletcher–Goldfarb–Shanno (L-BFGS) algorithm (Liu & Nocedal, 1989) to minimize the objective function. This algorithm offers an attractive way of approximating the inverse Hessian for a large-scale inverse problem by iteratively constructing approximations based on the changes in the model and the objective function gradient within a limited number of iterations (Pan et al., 2017).

Gradient of the objective function with respect to anisotropic parameters

The gradient of Φ_D with respect to the model parameter $m_j^{(n)}$ can be written as (Yang, 2023)

$$\frac{\partial \Phi_D}{\partial m_j^{(n)}} = -\Re \sum_s \sum_{\mathbf{x}_r} [W^2(\mathbf{x}_r) \Delta \mathbf{h}(\mathbf{x}_r, s)]^\dagger \frac{\partial}{\partial m_j^{(n)}} \mathbf{h}(\mathbf{x}_r, s), \quad (26)$$

where \Re takes the real part of a complex number and \dagger is the complex conjugate transpose operation.

To find the derivative of the magnetic field \mathbf{h} with respect to the model parameters $m_j^{(n)}$, we use an alternative expression of the \mathbf{h} in Equation (10) written by

$$\mathbf{h} = \mathcal{G}^{(H)} \mathbf{j}, \quad (27)$$

The operator $\mathcal{G}^{(H)}$ denotes the ‘heterogeneous background’ Green’s operator which outputs the magnetic field response of the media with heterogeneous conductivity distribution $\sigma(\mathbf{x})$ given the source vector \mathbf{j} (see Appendix A). The action of the operator $\mathcal{G}^{(H)}$ is defined as

$$\mathcal{G}^{(H)} = \mathcal{G}^{(0,H)} [\mathbf{I} - \Delta \sigma \mathcal{G}^{(0,E)}]^{-1}. \quad (28)$$

In this way, the magnetic field is expressed in terms of the source vector \mathbf{j} instead of the total electric field \mathbf{e} . By taking the derivative of the magnetic field in (27) with respect to the $m_j^{(n)}$, we obtain

$$\frac{\partial \mathbf{h}}{\partial m_j^{(n)}} = \mathcal{G}^{(H)} \frac{\partial \sigma}{\partial m_j^{(n)}} \mathbf{e}, \quad (29)$$

where, by using the definition in Equation (20), the derivative of the conductivity tensor with respect to the model parameter $m_j^{(n)}$ is given by

$$\begin{aligned} \frac{\partial \sigma}{\partial m_j^{(n)}} &= K^{(n)} \underbrace{\delta \sigma \mathbf{R}^T \mathbf{P}^{(j)} \cos [\mathbf{M}^{(n)}] \mathbf{R}}_{\tilde{\mathbf{C}}^{(n,j)}} \\ &= K^{(n)} \tilde{\mathbf{C}}^{(n,j)}. \end{aligned} \quad (30)$$

Substituting (29) and (30) into (26) results in the following expression of the gradient of the objective function with respect to the model parameter $m_j^{(n)}$:

$$\frac{\partial \Phi_D}{\partial m_j^{(n)}} = -\Re \sum_s \sum_{\mathbf{x}_r} [W^2 \Delta \mathbf{h}]^\dagger \mathcal{G}^{(H)} K^{(n)} \tilde{\mathbf{C}}^{(n,j)} \mathbf{e}. \quad (31)$$

For further details on the derivation, the interested reader is referred to Appendix B.

In the matrix-free implementation of the heterogeneous background Green’s operator (Hesford & Chew, 2010; Jakobsen et al., 2023), the action of the inverse operator $[\mathbf{I} - \Delta \sigma \mathcal{G}^{(0,E)}]^{-1}$ in Equation (28) can be calculated by solving the following linear systems of equations:

$$[\mathbf{I} - \Delta \sigma \mathcal{G}^{(0,E)}] \mathbf{e}^{(p)} = \mathbf{j}, \quad (32)$$

with $\mathbf{e}^{(p)}$ is an auxiliary field produced as the action of the inverse operator. Similar to the forward problem, this linear system of equations can also be solved using an iterative solver. Therefore, the computation of the gradient costs N times the forward solver call for each source configuration s with the formulation in (26). There is no additional solver cost for different receiver positions because $\mathbf{e}^{(p)}$ is defined for the entire space and the operator $\mathcal{G}^{(0,H)}$ only needs to output the magnetic field at the receiver positions.

Gradient formulation with adjoint field

By rearranging the terms, we show in Appendix C that we can express the gradient of the objective function for our choice of basis function in the form of

$$\frac{\partial \Phi_D}{\partial m_j^{(n)}} = -\Re \sum_s \int_{\Omega^{(n)}} [\mathbf{e}^{(a)}(\mathbf{x}, s)]^\dagger \tilde{\mathbf{C}}^{(n,j)} \mathbf{e}(\mathbf{x}, s) dV(\mathbf{x}), \quad (33)$$

with $\mathbf{e}^{(a)}$ the adjoint electric field, defined as

$$\mathbf{e}^{(a)} = \sum_{\mathbf{x}_r} [\mathcal{G}^{(H)}]^\dagger W^2 \Delta \mathbf{h}, \quad (34)$$

and the adjoint Green’s operator $[\mathcal{G}^{(H)}]^\dagger$ is written in the following:

$$[\mathcal{G}^{(H)}]^\dagger = [\mathbf{I} - \mathcal{G}^{(0,E)\dagger} \Delta \sigma]^{-1} [\mathcal{G}^{(0,H)}]^\dagger. \quad (35)$$

In this form, the gradient of the objective function is expressed in terms of the dot product between the adjoint and transformed total electric fields. The transformation of the total electric fields is governed by the matrix $\tilde{\mathbf{C}}^{(n,p)}$ defined in (30), which includes rotation and scaling of the electric field vector.

The adjoint fields are back-propagated from the receiver locations to the forward modelling domain with data misfit as the source using the adjoint of the ‘heterogeneous background’ Green’s operator. Taking the action of the inverse operator into account, the adjoint electric field is the solution

of the adjoint of the linear system in (32), namely,

$$\left[\mathbf{I} - \mathcal{G}^{(0,E)\dagger} \Delta \sigma \right] \mathbf{e}^{(a)} = \sum_{\mathbf{x}_r} \left[\mathcal{G}^{(0,H)} \right]^\dagger W^2 \Delta \mathbf{h}. \quad (36)$$

Similar to Equation (32), this linear system of equations can be solved using an iterative solver. Because the linear system of equations is the same for every adjoint source from different receiver positions, the right-hand side can be summed together to obtain the adjoint electric field in (36). Therefore, the calculation of the objective function's gradient in (33) costs additional forward solver calls for each transmitter configuration when using an iterative solver. This is desirable for a large-scale inverse problem, as it may be impossible to explicitly form the inverse operator matrix and store it in memory.

When the inversion grid is defined in the same way as the grid in the forward modelling window, the integral simply becomes the scaling of the dot product between the adjoint and transformed total electric fields with the volume of the local grid block Δv . Otherwise, it adds a summation operation over $\Omega^{(n)}(\mathbf{x})$ in addition to volume scaling. This implies that the computation of the gradient of the objective function for the reduced dimension (0D, 1D or 2D) can be computed by summing the gradient of the objective function defined in the 3D space over the direction where the model parameters are invariant.

Sequential inversion and assimilation

We invert the data for each logging position sequentially to mimic the inversion while drilling scenario. The information from the inverted model in the previous position to determine the initial starting model for the inversion using the data in the new position. In each logging position, we start the inversion by first finding the best 0D parameters and then introducing higher dimensional parameters when the inversion fails to reduce the data misfit. When the inversion is successful, the inversion results from all positions are assimilated according to the dimensionality of the inverted parameters. These processes are repeated for a new logging position until the end of the trajectory is reached. We set the stopping criteria based on the relative data residual defined as

$$\epsilon = \frac{\sum_s \sum_{\mathbf{x}_r} \|\Delta \mathbf{h}(\mathbf{x}_r, s)\|_2}{\sum_s \sum_{\mathbf{x}_r} \|\mathbf{h}^{(obs)}(\mathbf{x}_r, s)\|_2}. \quad (37)$$

To incorporate the information from the previous logging position, we use the sensitivity information derived from the inverted model at each logging position. We define the sensitivity as the derivative of the calculated magnetic field magnitude at the receiver positions with respect to the discrete

principal conductivity values:

$$\begin{aligned} S_j^{(n)} &= \frac{\partial}{\partial \sigma_j^{(n)}} \|\mathbf{h}(\mathbf{x}_r, s)\|_2^2 \\ &= \Re \sum_s \sum_{\mathbf{x}_r} \left[\mathcal{G}^{(H)} \frac{\partial \sigma}{\partial \sigma_j^{(n)}} \mathbf{e} \right]^\dagger \mathbf{h}. \end{aligned} \quad (38)$$

By using the definition of the conductivity tensor as the summation of discrete principal conductivity components

$$\sigma = \sum_{n=1}^N \sum_{j=1}^3 K^{(n)}(\mathbf{x}) \tilde{\mathbf{Q}}^{(j)} \sigma_j^{(n)}, \quad (39)$$

where $\tilde{\mathbf{Q}}^{(j)} = \mathbf{R}^T \mathbf{Q}^{(j)} \mathbf{R}$ and $\mathbf{Q}^{(j)}$ given by

$$\mathbf{Q}^{(1)} = \begin{bmatrix} 1 & 0 & 0 \\ 0 & 0 & 0 \\ 0 & 0 & 0 \end{bmatrix}, \quad \mathbf{Q}^{(2)} = \begin{bmatrix} 0 & 0 & 0 \\ 0 & 1 & 0 \\ 0 & 0 & 0 \end{bmatrix}, \quad \text{and} \quad \mathbf{Q}^{(3)} = \begin{bmatrix} 0 & 0 & 0 \\ 0 & 0 & 0 \\ 0 & 0 & 1 \end{bmatrix}, \quad (40)$$

Equation (38) can be rewritten in the similar manner as (33)

$$S_j^{(n)} = \Re \sum_s \int_{\Omega^{(n)}} [\tilde{\mathbf{e}}^{(a)}(\mathbf{x}, s)]^\dagger \tilde{\mathbf{Q}}^{(j)} \mathbf{e}(\mathbf{x}, s) dV(\mathbf{x}). \quad (41)$$

In this equation, $\tilde{\mathbf{e}}^{(a)}$ is the adjoint field with the magnetic fields as the source instead of the weighted data misfit, namely

$$\tilde{\mathbf{e}}^{(a)} = \sum_{\mathbf{x}_r} \left[\mathcal{G}^{(H)} \right]^\dagger \mathbf{h}. \quad (42)$$

The assimilated conductivity value is then a weighted mean of the inverted conductivity model from each logging position:

$$\bar{\sigma}_j^{(n)} = \left[\sum_{l=1}^L \bar{S}_j^{(n,l)} \sigma_j^{(n,l)} \right] \left[\sum_{l=1}^L \bar{S}_j^{(n,l)} \right]^{-1}, \quad (43)$$

where the superscripts l indicate the logging position. $\bar{S}_j^{(n)}$ is the absolute value of sensitivity normalized to its maximum value with a penalty term based on the model's relative residual, namely

$$\bar{S}_j^{(n)} = \min \left(1, \exp \left[\frac{\epsilon_{goal}}{\epsilon} \right] \right) \frac{|S_j^{(n)}|}{\max [|S_j^{(n)}|]}. \quad (44)$$

The idea is that the magnitude of the sensitivities is not distributed equally with space, and it typically decreases away from the transmitter and receiver positions. Therefore, the

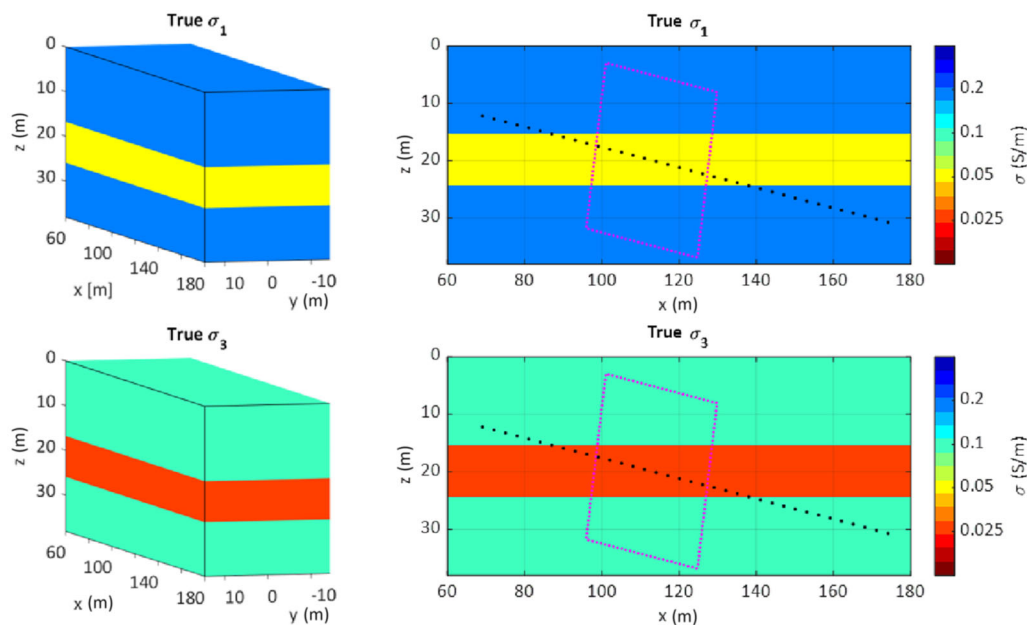


FIGURE 5 Conductivity distribution of the three horizontally layered model. The second column is the x - z slice at $y = 0$ m. Magenta boxes indicate the forward modelling window for a logging position.

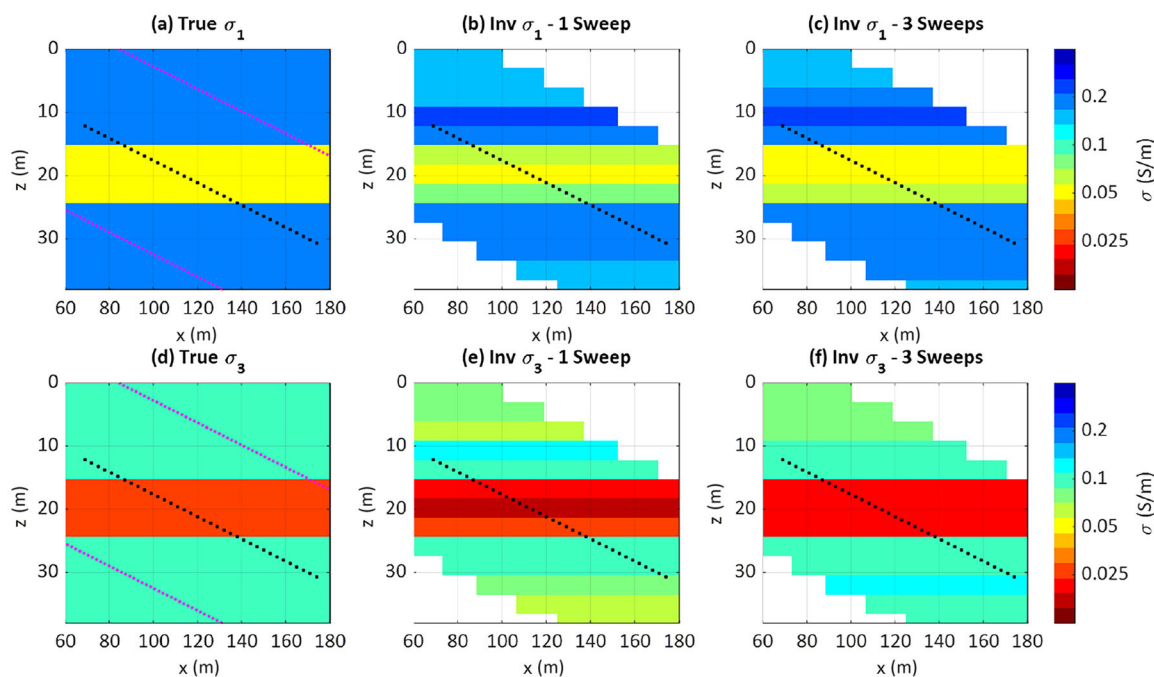


FIGURE 6 Horizontal and vertical conductivities. The first column shows the true model. The second and third columns show the inverted models for one and three sweeps, respectively. Black dots are the transmitter locations. Magenta dotted lines in the true models indicate the boundaries of the forward modelling window. Blank regions in the inverted models are outside the forward modelling window coverage.

assimilated conductivity values are set to be close to the inverted conductivity values obtained from the logging position with the highest sensitivity. The penalty term is used to reduce the weight of the model with large data misfits. We use the sensitivity value with respect to the principal conduc-

tivity values for the weighting because they are the physical parameters of interest and to remove the scaling effect due to transformation into different parameters. The assimilation strategy is as follows: the inverted conductivity is assimilated starting from groups of 1D results, then these groups

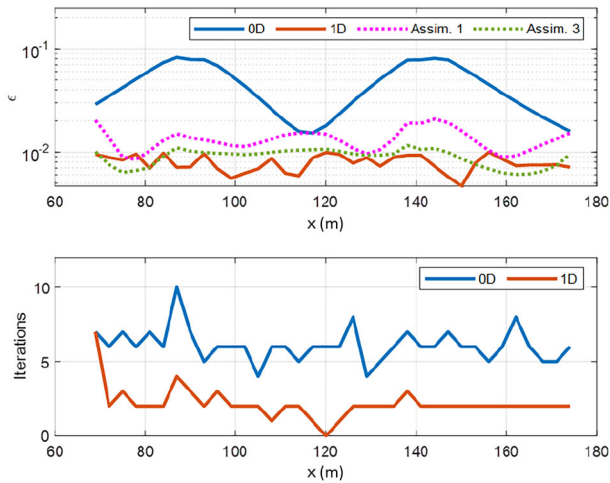


FIGURE 7 Relative residual for the inverted model (top) and number of iterations for inversion with different parameter dimensions (bottom). The magenta and green dotted lines indicate the relative residual of the assimilated inversion result from one and three sweeps, respectively. The x-axis represents the transmitter position.

are assimilated to groups of 2D results and finally 3D results if necessary.

NUMERICAL RESULTS AND DISCUSSION

We show two examples of our multi-dimensional parameter inversion while drilling across vertical transverse isotropy (VTI) media. The first example is an inversion of synthetic data generated from a horizontally layered model consisting of three VTI layers (Jahani et al., 2024). In the second example, we invert the synthetic data generated from a model with two-dimensional (2D) structures due to the presence of faults in the formation (Sviridov et al., 2023). To solve the linear system of equations for the forward modelling and gradient of the objective function, we use the BiCGSTAB algorithm (Van der Vorst, 1992) with a relative residual tolerance of 10^{-3} . The numerical experiments are implemented using MATLAB and executed on a laptop with an AMD Ryzen 7 4800H processor and NVIDIA GeForce RTX 3060 Laptop GPU.

Horizontally layered model

We tested our multi-dimensional parameter inversion method on a horizontally layered anisotropic medium consisting of three VTI layers, as shown in Figure 5. The top and bottom layers have the same horizontal and vertical conductivity, $\sigma_1 = 0.2$ S/m and $\sigma_3 = 0.1$ S/m, respectively. The middle layer is 9.144 m thick, and it is more resistive than the other two layers with $\sigma_1 = 0.05$ S/m and $\sigma_3 = 0.025$ S/m.

The induction tool moves through the layers from the top with a dip angle of 80 degrees. It has one transmitter with 12 kHz frequency and one receiver located 7.62 m behind the transmitter. The synthetic data are generated using a semi-analytical one-dimensional (1D) code (Shahriari et al., 2018), which we also used to validate our three-dimensional (3D) integral equation (IE) code (Saputera et al., 2024). We sampled the 1D data at 36 logging points with 3.048 m intervals along the drilling trajectory and inverted the data sequentially, one at a time, from the top left to the bottom right location, as shown by the black dots in the x - z slice in Figure 6. The 3D IE forward modelling window consists of $96 \times 96 \times 96$ grid blocks in all directions of the rotated axes with a grid size of $0.3048 \text{ m} \times 0.3048 \text{ m} \times 0.3048 \text{ m}$. We set a constant background conductivity $\sigma_0 = 0.1$ S/m and bound the conductivity values between the range of 0.01–1 S/m for all logging positions.

The centroids of the inversion grid are set in the range 0–213.36 m in the x -direction and 1.524–38.1 m in the z -direction with uniform intervals of 3.048 m in both directions. We specify the grid centroids in 2D in case 2D parameters are needed in the inversion. In the 1D parameter inversion, only the centroids in the z -direction are considered. For the stopping criteria of the inversion of a successful inversion, we set $\epsilon = 0.01$, which is equal to the expected forward model error of our 3D IE code compared to the 1D semi-analytical solution.

The results shown in the second column of the images in Figure 6 are obtained from one sweep of the sequential inversion and assimilation. This means that the data in each position is inverted once without considering the error in the other positions. The inverted conductivity models are combined using the assimilation scheme described in the previous section. Aside from representing the inverted models, the assimilated conductivity model is also used for the initial guess when new data are introduced. It took approximately 1 hour to invert 36 data sequentially from the starting to end position of the drilling trajectory.

Figure 7 shows the relative residual of the inverted model and the number of iterations taken in the inversion process in each position. In every position, the inversion workflow can reduce the data misfit below the defined goal using 1D parameters. The zero-dimensional (0D) parameter inversions are stopped when the data misfit cannot be reduced further within 10 iterations. As the inverted models are 1D everywhere, the assimilated result only shows a 1D structure. The relative residual conductivity from the assimilated inverted models is higher than the specified goal. However, it still shows a good agreement with the true model, with approximately 15% absolute normalized difference between the inverted and true model on average. This demonstrates that the assimilation is suitable for combining results obtained from inversion at multiple positions without having to invert the data all at once,

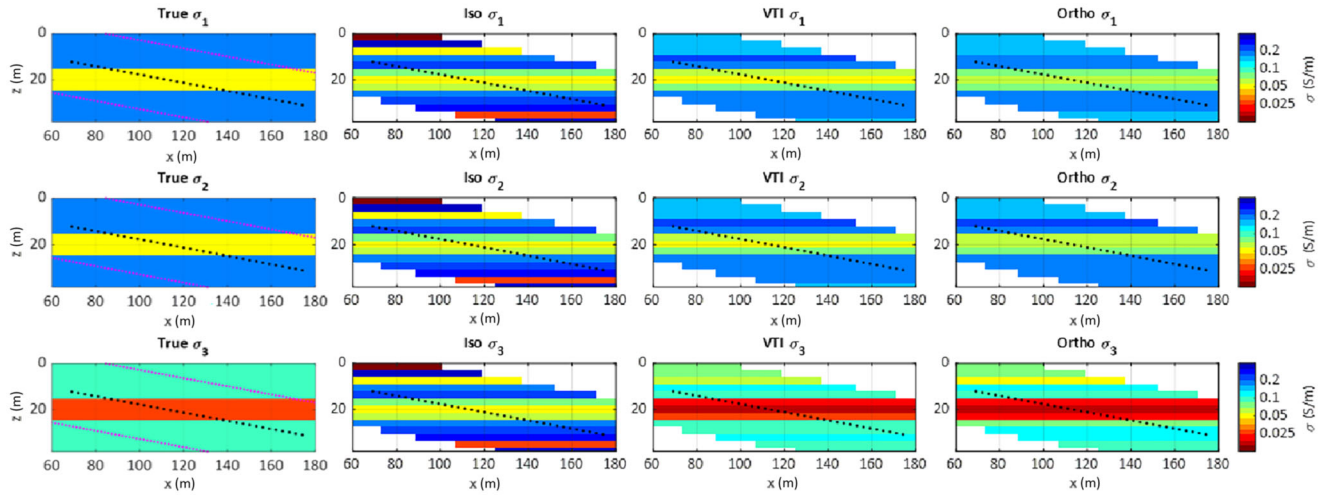


FIGURE 8 Inversion results with different types of anisotropic parameters. From left to right column: True model, inversion results with isotropic, VTI and orthorhombic parameters.

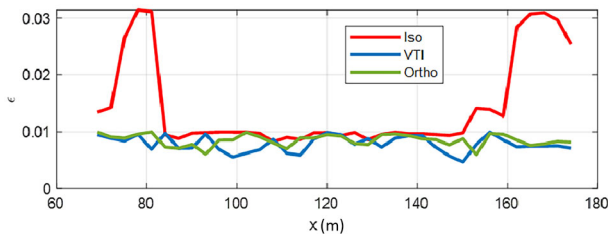


FIGURE 9 Relative residual for the inversion results using different types of anisotropy parameters.

which may be the case for inversion while drilling and/or inversion with limited computational resources and time.

The sequential inversion workflow, in principle, can be repeated until the data misfit goal is satisfied at every position. As the adaptive scheme produces information about the minimum parameter dimensions required to fit the data, this information can be used as prior knowledge for building the inversion grid in the next sweeps. The images in the third column in Figure 6 show the inversion and assimilation results after three sweeps where the average relative residual of the assimilated model for all positions is below 0.01. The results become closer to the true model compared to the results with only one sweep, where the absolute normalized difference between the inverted and true model is approximately 10% on average.

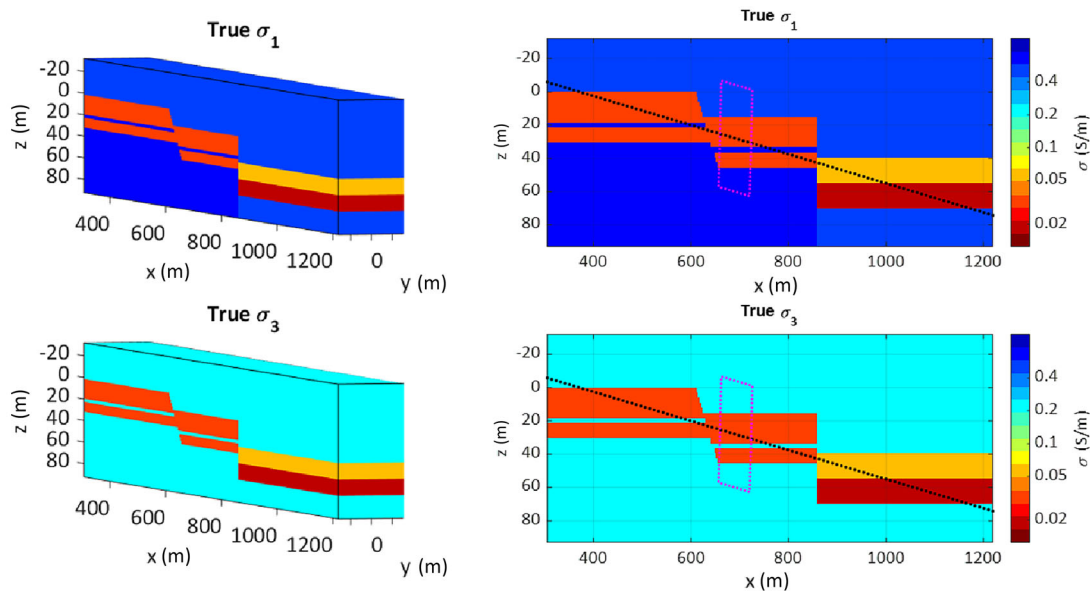


FIGURE 10 Conductivity distribution of the faulted anisotropic formation. The second column is the x - z slice at $y = 0$ m. Magenta boxes indicate the forward modelling window for a logging position.

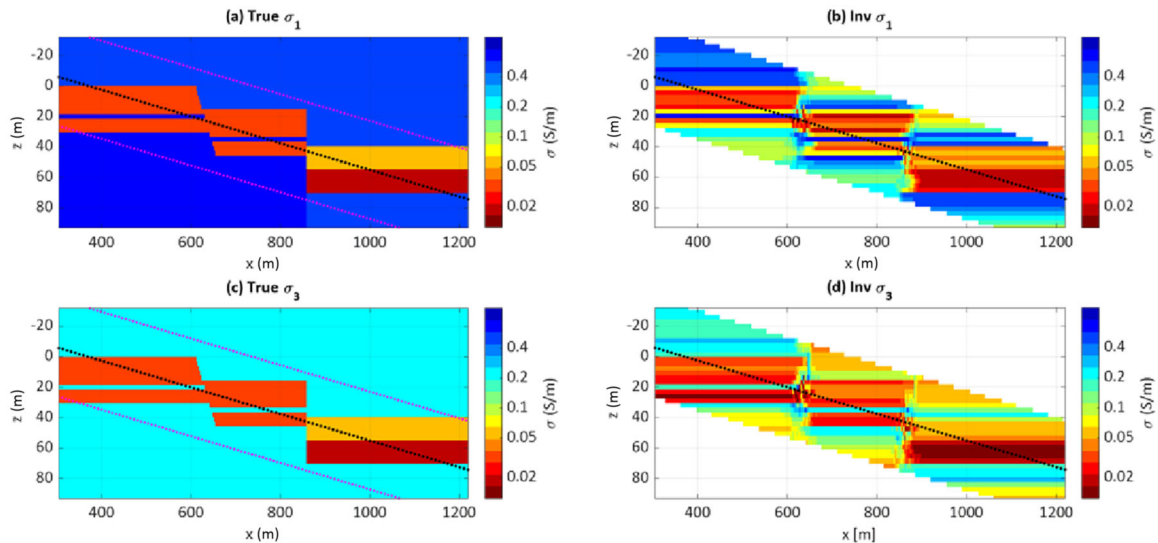


FIGURE 11 Horizontal and vertical conductivities. The left column shows the true model and the right column shows the inverted model. Black dots are the transmitter locations. Magenta dotted lines in the true models indicate the boundaries of the forward modelling window. Blank regions are outside of the forward modelling window.

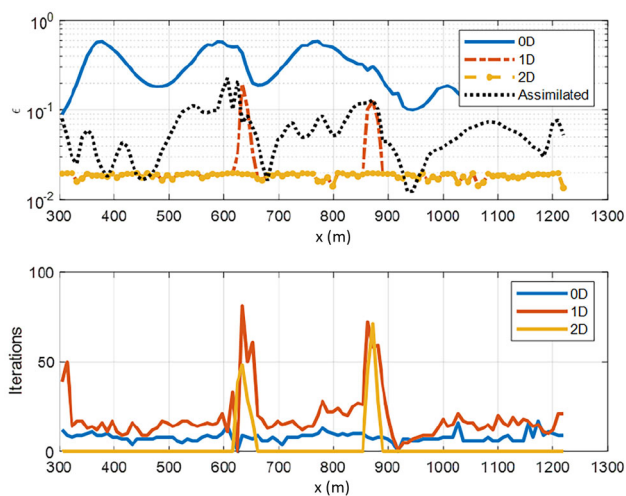


FIGURE 12 Relative residual for the inverted model (top) and number of iterations for inversion with different parameter dimensions (bottom). The black dotted line indicates the relative residual of the assimilated inversion result. The x -axis represents the transmitter position.

In practice, we may not know what type of anisotropy the medium in the subsurface around the borehole. To demonstrate the effect of anisotropic parameters on the inversion, we also invert the data of the horizontally layered model example using isotropic ($\sigma_1 = \sigma_2 = \sigma_3$) and orthorhombic ($\sigma_1 \neq \sigma_2 \neq \sigma_3$) parameters. In all cases, the maximum dimension of the inversion parameters is set to 1D to exclude the effect of using different model parameter dimensions in the inversion.

Figure 8 shows the assimilated conductivity profile from one sweep inversion using parameters with different types of anisotropy. The inversion with isotropic parameters is able to reconstruct the boundary of the middle layer of the true model fairly well. Aside from very low conductive layers at the top and bottom part of the inversion results, the conductivity values of the isotropic parameters are closer to the horizontal conductivities. This indicates different sensitivity of the tool configuration with different components of the conductivity tensor. Qualitatively, the inversion with orthorhombic parameters shows a pattern similar to the inversion of the VTI parameter.

Upon inspection of the relative residual, as displayed in Figure 9, the inversion with isotropic parameters is unable to find the conductivity model that fits the data within the desired misfit level when the transmitter is in the more conductive layer outside the middle layer. We hypothesize that this is the cause of inversion artifacts produced by the inversion algorithm, where spatial variations are introduced to compensate for the anisotropy effect. As expected, the misfit of inversion with orthorhombic parameters is below the desired goal, as there are more than enough parameters to represent the VTI condition.

Two-fault model

Figure 10 shows the conductivity model for this numerical example. The model consists of three blocks of horizontally layered conductivities separated by two faults. The induction tool trajectory has a dip angle of 85 degrees starting from the top left to the bottom right as shown in the x - z slice

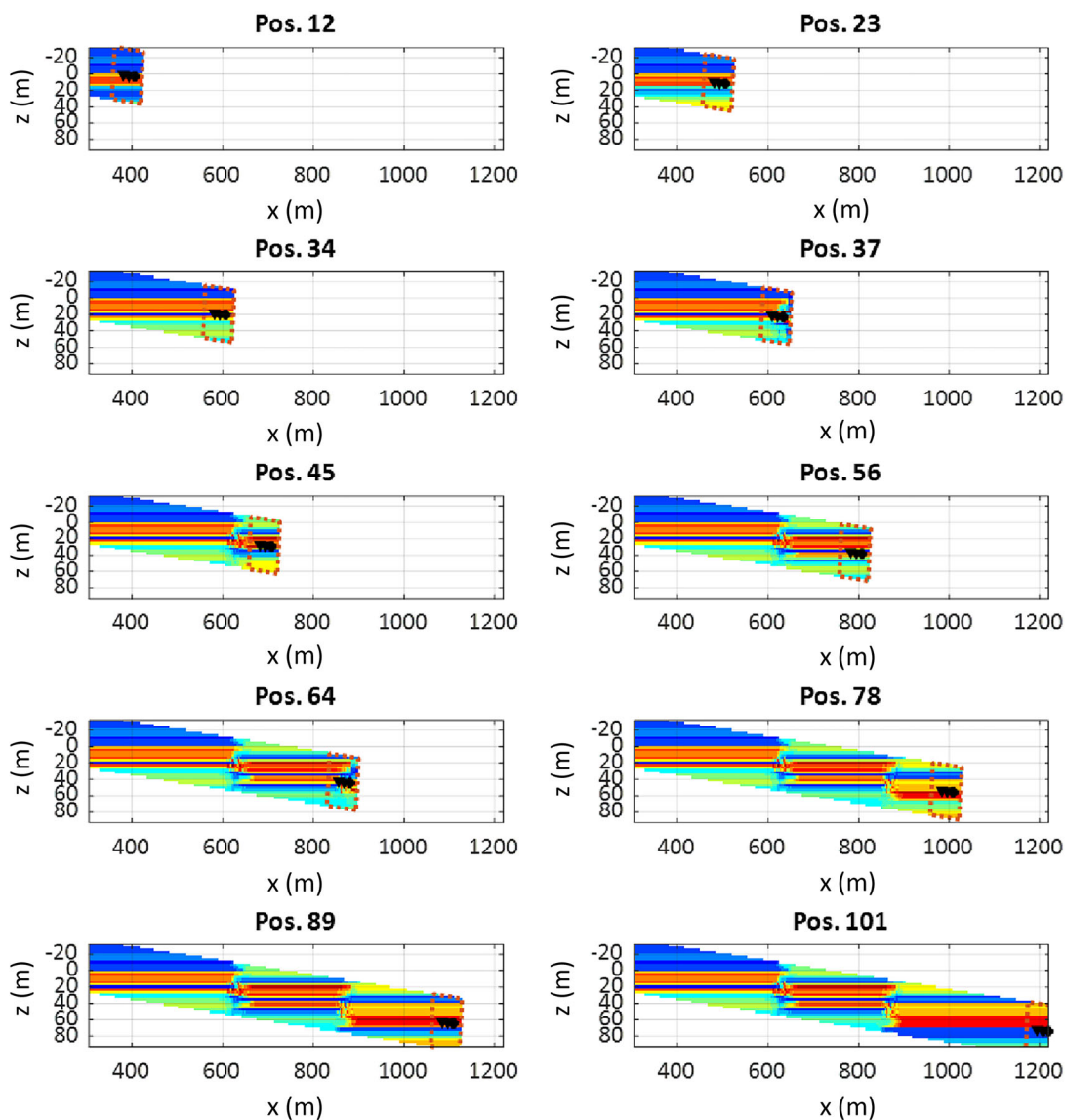


FIGURE 13 Snapshots of assimilated horizontal conductivity at several positions. Black dots and triangles are the transmitter and receiver positions, respectively. Dotted boxes indicate the coverage of the forward modelling window.

in Figure 10. The tool consists of one transmitter and two receivers. The first receiver is located 13.1 m behind the transmitter, and it contains data with frequencies of 24, 48 and 96 kHz. The second receiver has a spacing of 25.3 m from the transmitter location with frequencies of 6, 12 and 24 kHz.

The synthetic data are generated using our 3D IE code. The forward modelling window consists of $64 \times 64 \times 64$ grid blocks in all directions of the rotated axes with a grid size of $1 \text{ m} \times 1 \text{ m} \times 1 \text{ m}$. We set 352×42 inversion grid centroids in the range of 213.36–1280.2 m in the x -direction and -32.004 to 92.964 m in the z -direction with uniform intervals of 3.048 m in both directions. We set $\epsilon = 0.02$ as the stopping criteria of a successful inversion to not overfit the data for the inversion scenario with a noise level of approximately 2%.

Figure 11 shows the final inversion results obtained from one sweep of the sequential inversion. The data misfit of the inverted model and the number of inversion iterations at each position are displayed in Figure 12. The inversion workflow is able to reduce the data misfit below the target with 2D parameter inversions carried out at several positions. From the number of iterations in Figure 12, inversions with 2D parameters are carried out around $x = 640$ and 871 m. The number of iterations for inversions with 1D parameters around these locations is higher compared to the locations where the structure is dominantly 1D due to the algorithm's struggles to reduce the misfit with the inversion iterations. Overall, the inversion results show a good agreement with the true model. On average, the absolute normalized difference between the

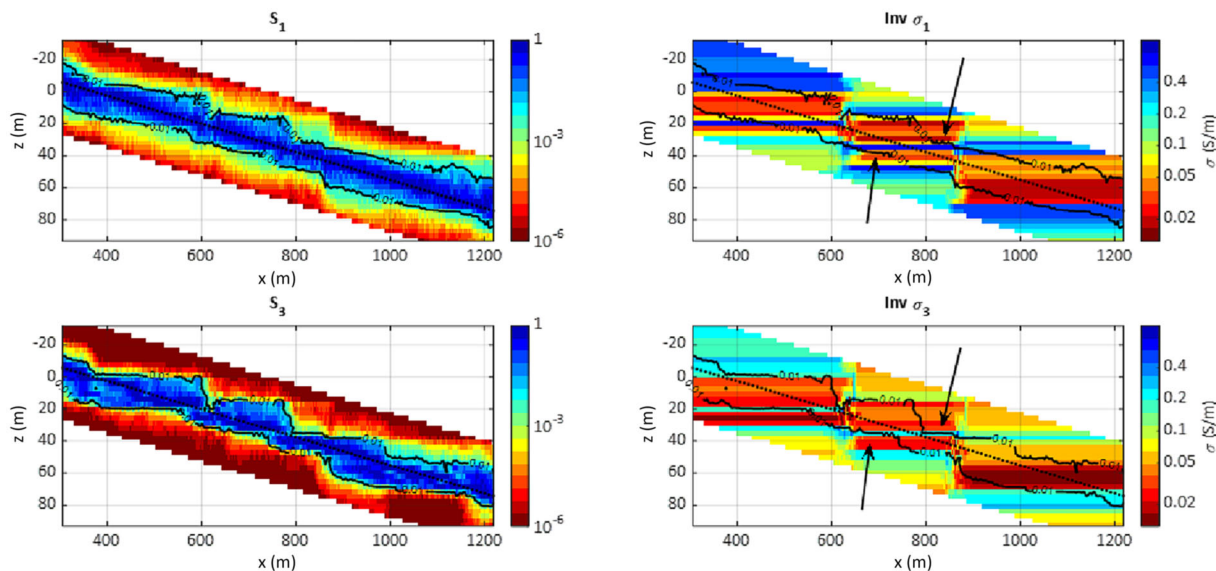


FIGURE 14 Left column: The sensitivities with respect to σ_1 and σ_3 . Right column: Inverted σ_1 and σ_3 . Dotted lines indicate the drilling trajectory. Solid lines correspond to the 0.01 contour line of the sensitivity values.

inverted and the true model is approximately 37%. It took approximately 15 hours to invert 101 data sequentially.

Figure 13 shows the changes in horizontal conductivity as the tool moves along the trajectory to illustrate the changes from 1D to 2D inversion parameters. Since the tool sensitivity is limited, the inverted result does not reconstruct the whole area all at once. The inversion results gradually reveal horizontal layering in the beginning. When the tool senses the lateral heterogeneity due to the vault, inversion with 1D parameters fails to reach the target 1D residual and lateral changes are allowed in the inversion with 2D parameters. As the tool becomes further away from the fault plane, the inversion algorithm can reach the goal with 1D parameters again.

Figure 14 shows the maximum relative sensitivity of the tools for all logging positions. Unlike estimation with skin depth calculated with homogeneous conductivity values, the sensitivity also varies laterally depending on the conductivity distributions. Qualitatively, these sensitivities show some interesting correlations with the inversion result. For example, the sensitivities drop rapidly in the thin conductive layers pointed out by the arrows. Then, if we look at the snapshot at position 45 in Figure 13, the resistive layer below the conductive layer is not revealed in the inversion result. After the tool crosses the thin conductive layer, see position number 56, then the layer is revealed.

CONCLUSION

We have developed an inversion workflow with multi-dimensional parameters in the framework of three-

dimensional (3D) forward modelling. The conductivity parameters in the voxels of the 3D simulation domain can be expressed as a sum of weighted basis functions. Using this principle, we define the appropriate objective function and gradient required for inverting the parameters in the zero-dimensional (0D), one-dimensional (1D) and two-dimensional (2D) grid systems. The inversion workflow starts by inverting the logging position for 0D parameters and using them as the initial guess for the inversion of 1D and 2D parameters. Then, the inversion results are assimilated through sensitivity-weighted averaging to create a single representation of the inverted models from multiple positions. To tackle the challenges in computational limitation, we implement a matrix-free integral equation method and adjoint method with the combination of the limited-memory Broyden–Fletcher–Goldfarb–Shanno (L-BFGS) as the inversion algorithm.

Numerical experiment results show that structural and anisotropy information of the true model can be recovered in the inversion process. An average model error of approximately 10% is achieved with multiple inversion sweeps in the first example. In the second example, the average model error is approximately 37% for one sweep inversion. In both cases, the dimensionality reduction in the inversion parameters helps stabilize the inversion results toward the most simple feasible solution even without having specified any regularization terms in the objective function. We additionally show that ignoring anisotropic parameters may lead to the generation of artefacts in the first example and the imposed dimensional constraint is not enough. In the second example, we also provide a qualitative analysis of the spatial distribution of the sensitivity to the 2D conductivity parameters, which is corre-

lated to the inverted conductivity evolution as the tool moves along the drilling trajectory.

Regarding computation time, it should be noted that we use 3D forward modelling for the inversion process. For 64^3 grid blocks, it took roughly 10 s to compute the magnetic field responses at the receiver with six transmitter frequencies and three transmitter orientations using our computer and implementation. Hence, it would take approximately 1000 s (~15 minutes) for an inversion with 100 function evaluations, which may not demonstrate the optimal use of the 3D solver in the inversion workflow. A more optimal approach would be to use a specialized forward modelling method according to the parameter dimension. Then, the workflow described in this study can be adapted. Alternatively, the formulation in this study can be used to implement matrix-free inversion with different basis functions that can describe simple 3D conductivity variations but are still simple to implement (e.g., polynomials, trigonometric functions or combinations). The question of how to design a good basis that promotes geologically feasible results and reduces the effect of regularization parameters tuning in the inversion process would be a valuable subject for future research.


ACKNOWLEDGEMENTS

This work is part of the Center for Research-Based Innovation DigiWells: Digital Well Center for Value Creation, Competitiveness and Minimum Environmental Footprint (NFR SFI project no. 309589; <https://DigiWells.no>). The centre is a cooperation of NORCE Norwegian Research Centre AS, the University of Stavanger, the Norwegian University of Science and Technology (NTNU) and the University of Bergen. It is funded by Aker BP, ConocoPhillips, Equinor, Lundin Energy, TotalEnergies, Vår Energi, Wintershall Dea and the Research Council of Norway. The one-dimensional data inverted in this work are from the code developed by the Formation Evaluation Research Consortium at UT Austin. The authors would like to acknowledge the involvement in three-dimensional geological interpretation for geosteering of wells project (project no. 336385).

DATA AVAILABILITY STATEMENT

Currently, the data and codes relating to this work are not freely available. We are considering publishing the codes with an open-source license in the future.

ORCID

Durra H. Saputera  <https://orcid.org/0000-0002-5500-0273>

Morten Jakobsen  <https://orcid.org/0000-0001-8861-1938>

REFERENCES

- Abubakar, A., Habashy, T., Druskin, V., Knizhnerman, L. & Alumbaugh, D. (2008) 2.5-D forward and inverse modeling for interpreting low-frequency electromagnetic measurements. *Geophysics*, 73(4), F165–F177.
- Abubakar, A., Habashy, T.M., Druskin, V., Knizhnerman, L. & Davdycheva, S. (2006) A 3D parametric inversion algorithm for triaxial induction data. *Geophysics*, 71(1), G1–G9.
- Alkhars, A., Achong, C., Fouda, M. & Bikchandaev, E. (2022) 3D inversion and 3D anisotropy analysis improve real-time decision-making process in complex clastic reservoirs. In *International Petroleum Technology Conference*. IPTC, D021S045R004.
- Antonsen, F., Danielsen, B.E., Jensen, K.R., Prymak-Moyle, M., Lotsberg, J.K., Teixeira De Oliveira, M.E. & Constable, M.V. (2022) What next after a decade with significant advances in the application of ultradeep azimuthal resistivity measurements?. *Petrophysics*, 63(6), 762–780.
- Barrett, R., Berry, M., Chan, T.F., Demmel, J., Donato, J., Dongarra, J., Eijkhout, V., Pozo, R., Romine, C. & Van der Vorst, H. (1994) *Templates for the solution of linear systems: Building blocks for iterative methods*. Philadelphia, PA: SIAM.
- Clegg, N., Eriksen, E., Best, K., Tøllefsen, I., Kotwicki, A. & Marchant, D. (2021) Mapping complex injectite bodies with multiwell electromagnetic 3D inversion data. *Petrophysics*, 62(1), 109–121.
- Elkhamry, A., Clegg, N., Taher, A. & Bikchandaev, E. (2023) The first successful azimuthal well placement utilizing real-time azimuthal resistivity measurements and ultra-deep 3D inversion. In *International Petroleum Technology Conference*, D012S006R001. IPTC.
- Elkhamry, A., Taher, A., Bikchandaev, E. & Fouda, M. (2022) Real-time 3d anisotropy analysis enables lithology identification at distance. In *SPWLA Annual Logging Symposium*, D041S009R004. Houston, TX: SPWLA.
- Fang, S., Gao, G. & Verdin, C.T. (2006) Efficient 3D electromagnetic modelling in the presence of anisotropic conductive media, using integral equations. *Exploration Geophysics*, 37(3), 239–244.
- Gao, G. (2006) Simulation of borehole electromagnetic measurements in dipping and anisotropic rock formations and inversion of array induction data. PhD thesis, The University of Texas at Austin.
- Gibson, W.C. (2021) *The method of moments in electromagnetics*. Boca Raton, FL: CRC Press.
- Greenhalgh, S., Zhou, B., Greenhalgh, M., Marescot, L. & Wiese, T. (2009) Explicit expressions for the Fréchet derivatives in 3D anisotropic resistivity inversion. *Geophysics*, 74(3), F31–F43.
- Hesford, A.J. & Chew, W.C. (2010) Fast inverse scattering solutions using the distorted born iterative method and the multilevel fast multipole algorithm. *The Journal of the Acoustical Society of America*, 128(2), 679–690.
- Jahani, N., Torres-Verdín, C. & Hou, J. (2024) Limits of three-dimensional target detectability of logging while drilling deep-sensing electromagnetic measurements from numerical modelling. *Geophysical Prospecting*, 72(3), 1146–1162.
- Jahani, N., Torres-Verdín, C., Hou, J. & Tveranger, J. (2023) Limits of 3D detectability and resolution of LWD Deep-sensing borehole electromagnetic measurements acquired in the Norwegian Continental Shelf. In *SPWLA Annual Logging Symposium*, D041S008R005. Houston, TX: SPWLA.
- Jakobsen, M., Ivan, E., Psencik, I. & Ursin, B. (2020) Transition operator approach to seismic full-waveform inversion in arbitrary anisotropic elastic media. *Communications in Computational Physics*, 28(1), 297–327.
- Jakobsen, M. & Tveit, S. (2018) Distorted Born iterative T-matrix method for inversion of CSEM data in anisotropic media. *Geophysical Journal International*, 214(3), 1524–1537.

- Jakobsen, M., Xiang, K. & van Dongen, K.W. (2023) Seismic and medical ultrasound imaging of velocity and density variations by nonlinear vectorial inverse scattering. *The Journal of the Acoustical Society of America*, 153(5), 3151–3151.
- Kong, W., Tan, H., Lin, C., Unsworth, M., Lee, B., Peng, M., Wang, M. & Tong, T. (2021) Three-dimensional inversion of magnetotelluric data for a resistivity model with arbitrary anisotropy. *Journal of Geophysical Research: Solid Earth*, 126(8), e2020JB020562.
- Liu, D.C. & Nocedal, J. (1989) On the limited memory BFGS method for large scale optimization. *Mathematical Programming*, 45(1), 503–528.
- Moran, J. & Gianzero, S. (1979) Effects of formation anisotropy on resistivity-logging measurements. *Geophysics*, 44(7), 1266–1286.
- Newman, G.A. & Alumbaugh, D.L. (2002) Three-dimensional induction logging problems, part 2: A finite-difference solution. *Geophysics*, 67(2), 484–491.
- Omar, S., Salim, D., Zaslavsky, M. & Liang, L. (2024) High-resolution 3D reservoir mapping and geosteering using voxel-based inversion processing of Udar measurements. In *SPWLA Annual Logging Symposium*, D041S016R001. Houston, TX: SPWLA.
- Pan, W., Innanen, K.A. & Liao, W. (2017) Accelerating Hessian-free Gauss-Newton full-waveform inversion via L-BFGS preconditioned conjugate-gradient algorithm. *Geophysics*, 82(2), R49–R64.
- Pardo, D. & Torres-Verdín, C. (2015) Fast 1D inversion of logging-while-drilling resistivity measurements for improved estimation of formation resistivity in high-angle and horizontal wells. *Geophysics*, 80(2), E111–E124.
- Pek, J. & Santos, F.A. (2002) Magnetotelluric impedances and parametric sensitivities for 1-D anisotropic layered media. *Computers & Geosciences*, 28(8), 939–950.
- Petersen, K.B., Pedersen, M.S., et al., (2012) *The matrix cookbook*. Technical University of Denmark.
- Rong, Z., Liu, Y., Yin, C., Wang, L., Ma, X., Qiu, C., Zhang, B., Ren, X., Su, Y. & Weng, A. (2022) Three-dimensional magnetotelluric inversion for arbitrarily anisotropic earth using unstructured tetrahedral discretization. *Journal of Geophysical Research: Solid Earth*, 127(8), e2021JB023778.
- Saad, Y. (2003) *Iterative methods for sparse linear systems*. Philadelphia, PA: SIAM.
- Saputera, D.H., Jakobsen, M., van Dongen, K.W., Jahani, N., Eikrem, K.S. & Alyaev, S. (2024) 3-D induction log modelling with integral equation method and domain decomposition pre-conditioning. *Geophysical Journal International*, 236(2), 834–848.
- Saputra, W., Ambia, J., Torres-Verdín, C., Davydycheva, S., Druskin, V., & Zimmerling, J. (2024) Adaptive multidimensional inversion for borehole ultra-deep azimuthal resistivity. In *SPWLA Annual Logging Symposium*, D041S013R005. Houston, TX: SPWLA.
- Shahriari, M., Rojas, S., Pardo, D., Rodríguez-Rozas, A., Bakr, S.A., Calo, V.M. & Muga, I. (2018) A numerical 1.5 D method for the rapid simulation of geophysical resistivity measurements. *Geosciences*, 8(6), 225.
- Sviridov, M., Kushnir, D., Mosin, A., Nemuschenko, D. & Rabinovich, M. (2023) High-performance stochastic inversion for real-time processing of LWD ultra-deep azimuthal resistivity data. In *SPWLA Annual Logging Symposium*, D041S014R009. Houston, TX: SPWLA.
- Van den Berg, P. & Van der Horst, M. (1995) Nonlinear inversion in induction logging using the modified gradient method. *Radio Science*, 30(5), 1355–1369.
- Van den Berg, P.M. & Abubakar, A. (2001) Contrast source inversion method: state of art. *Progress in Electromagnetics Research*, 34(11), 189–218.
- Van der Vorst, H.A. (1992) Bi-CGSTAB: a fast and smoothly converging variant of bi-cg for the solution of nonsymmetric linear systems. *SIAM Journal on Scientific and Statistical Computing*, 13(2), 631–644.
- Wang, B., Liu, J., Hu, X., Liu, J., Guo, Z. & Xiao, J. (2021) Geophysical electromagnetic modeling and evaluation: a review. *Journal of Applied Geophysics*, 194, 104438.
- Wilson, G., Marchant, D., Haber, E., Clegg, N., Zurcher, D., Rawsthorpe, L. & Kunas, J. (2019) Real-time 3D inversion of ultra-deep resistivity logging-while-drilling data. In *SPE Annual Technical Conference and Exhibition*. OnePetro.
- Wu, H.-H., Wu, D., Ma, J., Yan, T., Lozinsky, C. & Bittar, M. (2024) Enhancing local anisotropy characterization with ultra-deep azimuthal resistivity measurements. In *SPWLA Annual Logging Symposium*, D041S013R001. Houston, TX: SPWLA.
- Yang, P. (2023) 3D fictitious wave domain CSEM inversion by adjoint source estimation. *Computers & Geosciences*, 180, 105441.
- Yin, C. (2000) Geoelectrical inversion for a one-dimensional anisotropic model and inherent non-uniqueness. *Geophysical Journal International*, 140(1), 11–23.
- Zhdanov, M.S. (2009) *Geophysical electromagnetic theory and methods*. Amsterdam: Elsevier.
- Zwamborn, P. & Van Den Berg, P.M. (1992) The three dimensional weak form of the conjugate gradient FFT method for solving scattering problems. *IEEE Transactions on Microwave Theory and Techniques*, 40(9), 1757–1766.

How to cite this article: Saputera, D.H., Jakobsen, M., van Dongen, K.W.A. & Jahani, N. (2025) Sequential multi-dimensional parameter inversion of induction logging data. *Geophysical Prospecting*, 73, 1315–1332. <https://doi.org/10.1111/1365-2478.70017>

APPENDIX A: HETEROGENEOUS BACKGROUND GREEN'S OPERATOR

The Green's function is defined as the response of an impulse function (Zhdanov, 2009). For example, the electric field in the homogeneous isotropic medium with conductivity σ_0 is defined as

$$\mathbf{e}^{(0)} = \mathcal{G}^{(0,E)} \mathbf{j}, \quad (\text{A.1})$$

where the upper-scripts (0) indicate a homogeneous isotropic background and \mathbf{j} is the electric source vector. We use an electric source as an example because the scattered field depends on the conductivity contrast multiplied by the electric fields as stated in Equation (3).

The electric field in an arbitrary heterogeneous background medium with conductivity $\sigma(\mathbf{x})$ is obtained by solving the linear system of equations in (8). This equation can be written as a function of the electric source vector \mathbf{j} in a similar form as

(A.1):

$$\mathbf{e} = \mathcal{G}^{(E)} \mathbf{j}, \quad (\text{A.2})$$

where

$$\mathcal{G}^{(E)} = [\mathbf{I} - \mathcal{G}^{(0,E)} \Delta \sigma]^{-1} \mathcal{G}^{(0,E)}, \quad (\text{A.3})$$

is defined as the heterogeneous background Green's tensor operator for the electric field due to an impulse source.

By taking the curl of the Equation (A.2) and division by $i\omega\mu_0$, we can obtain the expression of the magnetic field in the heterogeneous background medium as

$$\begin{aligned} \mathbf{h} &= \frac{1}{i\omega\mu_0} \nabla \times \mathcal{G}^{(E)} \mathbf{j} \\ &= \mathcal{G}^{(H)} \mathbf{j}. \end{aligned} \quad (\text{A.4})$$

Rearranging the terms in Equation (A.3) using the following identity (Jakobsen et al., 2020; Petersen et al., 2012):

$$(\mathbf{I} - \mathbf{G}\mathbf{V})^{-1} \mathbf{G} = \mathbf{G}(\mathbf{I} - \mathbf{V}\mathbf{G})^{-1}, \quad (\text{A.5})$$

the Green's tensor operator for the magnetic field in a heterogeneous medium due to an electric source can be written as

$$\mathcal{G}^{(H)} = \frac{1}{i\omega\mu_0} \nabla \times \mathcal{G}^{(0,E)} [\mathbf{I} - \Delta \sigma \mathcal{G}^{(0,E)}]^{-1}, \quad (\text{A.6})$$

which is equivalent to

$$\mathcal{G}^{(H)} = \mathcal{G}^{(0,H)} [\mathbf{I} - \Delta \sigma \mathcal{G}^{(0,E)}]^{-1}. \quad (\text{A.7})$$

APPENDIX B: DERIVATION OF THE OBJECTIVE FUNCTION GRADIENT

To find the gradient of the objective function in (23) with respect to the model parameter $m_j^{(n)}$, we first find the derivative of the magnetic field Green's tensor operator $\mathcal{G}^{(H)}$ with respect to $m_j^{(n)}$ by rewriting Equation (A.7) in the form of

$$\mathcal{G}^{(H)} = \mathcal{G}^{(0,H)} + \mathcal{G}^{(H)} \Delta \sigma \mathcal{G}^{(0,E)}. \quad (\text{B.1})$$

By taking the derivative on both sides of the Equation (B.1) with respect to $m_j^{(n)}$, we obtain

$$\frac{\partial \mathcal{G}^{(H)}}{\partial m_j^{(n)}} = \frac{\partial \mathcal{G}^{(0,H)}}{\partial m_j^{(n)}} \Delta \sigma \mathcal{G}^{(0,E)} + \mathcal{G}^{(H)} \frac{\partial \Delta \sigma}{\partial m_j^{(n)}} \mathcal{G}^{(0,E)}. \quad (\text{B.2})$$

Next, we collect the partial derivative terms of $\mathcal{G}^{(H)}$ on the left side and obtain

$$\frac{\partial \mathcal{G}^{(H)}}{\partial m_j^{(n)}} [\mathbf{I} - \Delta \sigma \mathcal{G}^{(0,E)}] = \mathcal{G}^{(H)} \frac{\partial \Delta \sigma}{\partial m_j^{(n)}} \mathcal{G}^{(0,E)}, \quad (\text{B.3})$$

or

$$\frac{\partial \mathcal{G}^{(H)}}{\partial m_j^{(n)}} = \mathcal{G}^{(H)} \frac{\partial \Delta \sigma}{\partial m_j^{(n)}} \mathcal{G}^{(0,E)} [\mathbf{I} - \Delta \sigma \mathcal{G}^{(0,E)}]^{-1}. \quad (\text{B.4})$$

Using the magnetic field definition in (A.4), the derivative of the magnetic field \mathbf{h} with respect to $m_j^{(n)}$ is defined as

$$\begin{aligned} \frac{\partial \mathbf{h}}{\partial m_j^{(n)}} &= \frac{\partial \mathcal{G}^{(H)}}{\partial m_j^{(n)}} \mathbf{j} \\ &= \mathcal{G}^{(H)} \frac{\partial \Delta \sigma}{\partial m_j^{(n)}} \mathcal{G}^{(0,E)} [\mathbf{I} - \Delta \sigma \mathcal{G}^{(0,E)}]^{-1} \mathbf{j}. \end{aligned} \quad (\text{B.5})$$

Rearranging the terms using the identity in (A.5), we obtain

$$\frac{\partial \mathbf{h}}{\partial m_j^{(n)}} = \mathcal{G}^{(H)} \frac{\partial \Delta \sigma}{\partial m_j^{(n)}} \underbrace{[\mathbf{I} - \mathcal{G}^{(0,E)} \Delta \sigma]^{-1} \mathcal{G}^{(0,E)} \mathbf{j}}_{\mathbf{e}}, \quad (\text{B.6})$$

where the terms on the brace are the total electric field \mathbf{e} based on Equations (A.2) and (A.3). Finally, substituting (B.6) into (26) gives us the expression for the gradient of the objective function with respect to $m_j^{(n)}$ in the following:

$$\frac{\partial \Phi_D}{\partial m_j^{(n)}} = -\Re \sum_s \sum_{\mathbf{x}_r} [W^2(\mathbf{x}_r) \Delta \mathbf{h}(\mathbf{x}_r, s)]^\dagger \mathcal{G}^{(H)} \frac{\partial \Delta \sigma}{\partial m_j^{(n)}} \mathbf{e}. \quad (\text{B.7})$$

APPENDIX C: GRADIENT FORMULATION WITH THE ADJOINT FIELD

We can write (B.7) explicitly as shown below

$$\begin{aligned} \frac{\partial \Phi_D}{\partial m_j^{(n)}} &= -\Re \sum_s \sum_{\mathbf{x}_r} [W^2(\mathbf{x}_r) \Delta \mathbf{h}(\mathbf{x}_r, s)]^\dagger \\ &\quad \cdot \int_{\Omega} \mathbf{G}^{(H)}(\mathbf{x}, \mathbf{x}_r, \omega) \frac{\partial \Delta \sigma}{\partial m_j^{(n)}}(\mathbf{x}) \mathbf{e}(\mathbf{x}, s) dV(\mathbf{x}). \end{aligned} \quad (\text{C.1})$$

By rearranging the integral and summation, we obtain

$$\begin{aligned} \frac{\partial \Phi_D}{\partial m_j^{(n)}} &= -\Re \sum_s \int_{\Omega} \left(\sum_{\mathbf{x}_r} [W^2(\mathbf{x}_r) \Delta \mathbf{h}(\mathbf{x}_r, s)]^\dagger \mathbf{G}^{(H)}(\mathbf{x}, \mathbf{x}_r, \omega) \right) \\ &\quad \cdot \frac{\partial \Delta \sigma}{\partial m_j^{(n)}}(\mathbf{x}) \mathbf{e}(\mathbf{x}, s) dV(\mathbf{x}) \\ &= -\Re \sum_s \int_{\Omega} [\mathbf{e}^{(a)}(\mathbf{x}, s)]^\dagger \frac{\partial \Delta \sigma}{\partial m_j^{(n)}}(\mathbf{x}) \mathbf{e}(\mathbf{x}, s) dV(\mathbf{x}), \end{aligned} \quad (\text{C.2})$$

where the adjoint field $\mathbf{e}^{(a)}$ is defined by

$$\mathbf{e}^{(a)} = \sum_{\mathbf{x}_r} [\mathbf{G}^{(H)}(\mathbf{x}, \mathbf{x}_r, \omega)]^\dagger \mathcal{W}^2(\mathbf{x}_r) \Delta \mathbf{h}(\mathbf{x}_r, s), \quad (\text{C.3})$$

and $\mathbf{G}^{(H)}$ is the dyadic Green's function for the heterogeneous background medium with conductivity $\sigma(\mathbf{x})$. Applying the adjoint integral equation method of Jakobsen et al. (2023), we use the physical interpretation of $\mathbf{G}^{(H)}$ and the adjoint field can be found by solving the linear system of equation in (36).

Inserting the term $\frac{\partial \sigma}{\partial m_j^{(n)}}$ for the conductivity tensor defined in (20), the gradient of the objective function is written as

$$\begin{aligned} \frac{\partial \Phi_D}{\partial m_j^{(n)}} &= -\Re \sum_s \int_{\Omega} K^{(n)}(\mathbf{x}) [\mathbf{e}^{(a)}(\mathbf{x}, s)]^\dagger \tilde{\mathbf{C}}^{(n,j)} \mathbf{e}(\mathbf{x}, s) dV(\mathbf{x}) \\ &= -\Re \sum_s \int_{\Omega^{(n)}} [\mathbf{e}^{(a)}(\mathbf{x}, s)]^\dagger \tilde{\mathbf{C}}^{(n,j)} \mathbf{e}(\mathbf{x}, s) dV(\mathbf{x}), \end{aligned} \quad (\text{C.4})$$

where the matrix $\tilde{\mathbf{C}}^{(n,j)}$ is defined in (30). Because we use the block indicator function described in (16) as the basis function, the domain of the volumetric integral changes from Ω to $\Omega^{(n)}$ where the basis function is non-zero.